

This is an Open Access document downloaded from ORCA, Cardiff University's institutional repository: <https://orca.cardiff.ac.uk/id/eprint/94488/>

This is the author's version of a work that was submitted to / accepted for publication.

Citation for final published version:

Du, Jonathan J., Váradi, Linda, Williams, Peter A., Groundwater, Paul W., Overgaard, Jacob, Platts, James Alexis and Hibbs, David E. 2016. An analysis of the experimental and theoretical charge density distributions of the piroxicam-saccharin co-crystal and its constituents. RSC Advances 6 (85) , pp. 81578-81590. 10.1039/C6RA10411H

Publishers page: <http://dx.doi.org/10.1039/C6RA10411H>

Please note:

Changes made as a result of publishing processes such as copy-editing, formatting and page numbers may not be reflected in this version. For the definitive version of this publication, please refer to the published source. You are advised to consult the publisher's version if you wish to cite this paper.

This version is being made available in accordance with publisher policies. See <http://orca.cf.ac.uk/policies.html> for usage policies. Copyright and moral rights for publications made available in ORCA are retained by the copyright holders.



**An analysis of the experimental and theoretical charge density distributions of the piroxicam-saccharin co-crystal and its constituents**

**Jonathan J. Du,<sup>1</sup> Linda Váradi,<sup>1</sup> Paul W. Groundwater,<sup>1</sup> Jacob Overgaard,<sup>3</sup> James A. Platts<sup>2</sup> and David E. Hibbs<sup>1\*</sup> and Peter A. Williams,<sup>1,4</sup>**

*<sup>1</sup>Faculty of Pharmacy, University of Sydney, NSW 2006 Australia*

*<sup>2</sup>School of Chemistry, Cardiff University, Cardiff, CF10 3AT, UK.*

*<sup>3</sup>Department of Chemistry, Center for Materials Crystallography, Aarhus University, Langelandsgade 140, Aarhus C, 8000, Denmark*

*<sup>4</sup>School of Science and Health, University of Western Sydney, Locked Bag 1797, Penrith, NSW, 2751*

*\*Corresponding author: David E. Hibbs, david.hibbs@sydney.edu.au*

## Abstract

Experimental and theoretical charge density analyses of piroxicam (**1**), saccharin (**2**) and their 1:1 co-crystal complex (**3**) have been carried out. Electron density distribution (EDD) was determined through the use of high-resolution single crystal X-ray diffraction and the data were modelled using the conventional multipole model of electron density according to the Hansen-Coppens formalism. A method for optimising the core density refinement of sulfur atoms is discussed, with emphasis on the reduction of residual electron density that is typically associated with this atom. The asymmetric unit of complex (**3**) contains single molecules of saccharin and the zwitterionic form of piroxicam. These are held together by weak interactions (hydrogen bonds,  $\pi$ - $\pi$  and van der Waals interactions), ranging in strength from 4 to 160 kJmol<sup>-1</sup>, working together to stabilise the complex;. analysis of the molecular electrostatic potential (MEP) of the complexes showed electron redistribution within the co-crystal, facilitating the formation of these generally weak interactions. Interestingly, in the zwitterionic form of piroxicam, the charge distribution reveals that the positive and negative charges are not associated with the formal charges normally associated with this description, but are distributed over adjacent molecular fragments. The use of anisotropic displacement parameters (ADPs) for hydrogen atoms in the multipole model was also investigated but no improvement in the quality of the topological analysis was found.

## Introduction

Piroxicam, commercially known as Feldene or Mobili, is a non-steroidal anti-inflammatory drug (NSAID) and is used for a wide range of indications including rheumatoid arthritis, osteoarthritis and various other superficial sporting injuries(1). Its mechanism of action is the non-selective inhibition of the cyclooxygenase (COX) 1 and 2 pathways to inhibit the production in prostaglandins involved in inflammatory and pain responses in response to injury. The non-selective inhibition exhibited by piroxicam results in an unfavourable adverse effect profile, with one of the more pressing issues being gastrointestinal (GI) damage via disruption of the integrity of the gastric mucosa and prevention of its regeneration(2). This has been one of the major reasons for piroxicam being less commonly prescribed than selective COX 2 inhibitors such as meloxicam, which has more favourable adverse effect profiles.

A potential solution to this problem was raised in 2013 *via* the use of an inclusion complex (piroxicam- $\beta$ -Cyclodextrin)(2), which was found to have less GI side effects compared to free piroxicam. Co-crystallisation is a similar solution to the problem and has previously been investigated by Banerjee *et al.* through the piroxicam-saccharin co-crystal(3), which has been found to modify the physicochemical properties of piroxicam compared to free piroxicam. The development of an economically viable and universal method to improve physicochemical properties of an active pharmaceutical ingredient (API) without changing its activity has been at the forefront of research in the pharmaceuticals area and has garnered widespread interest from both academia and industry.(4) Co-crystals, defined as crystals composed of two or more components that are solid at room temperature(5) and pharmaceutical co-crystals where one of the components is an API are believed by many to be a viable and cost effective solution to this problem.

Pharmaceutical co-crystals, by improving physicochemical, pharmacokinetic and pharmacodynamics properties of APIs will allow pharmaceutical companies to bring more drugs to the market in a shorter period of time. This significantly reduces research and design costs, particularly as poor physicochemical properties (such as solubility, dissolution rate, bioavailability, chemical stability, and hygroscopicity) are the primary reason for over 80% of APIs failing to reach the market.<sup>(6)</sup> Furthermore, improved physicochemical properties will allow drugs to be made into more acceptable dose forms such as tablets and this will lead to increased adherence and subsequently improved patient health outcomes. Moreover, novel formulations which allow new patents or to extend the life of older patents are of great interest to pharmaceutical companies. Co-crystals are considered to fulfil all the criteria for patentability, namely novelty, utility and non-obviousness,<sup>(4, 7)</sup> even though the API is identical.

This paper aims to examine the abovementioned co-crystal at the electronic level to determine the mechanism behind the change in physicochemical activity of the co-crystallised piroxicam compared to its free form. Nguyen *et al.* recently published research regarding the use of density functional theory (DFT) and atoms in molecules (AIM) theory<sup>(8)</sup> to analyse EDD in experimental and theoretical models to examine weak interactions such as hydrogen bonds (HBs),  $\pi$ - $\pi$  stacking and van der Waals interactions present in biologically significant systems, including host-receptor complexes.<sup>(9, 10)</sup> They concluded that an increased understanding of the electron and hence energy distribution in such interactions will lead to continued improvements in the drug design and development process, potentially resulting in the development of more efficacious and less toxic therapeutics. Following on from these benefits offered by pharmaceutical co-crystals in the development of efficacious and non-toxic therapeutics, a more detailed look at the weak interactions between API and co-former within a crystalline environment *via* an EDD study is warranted to increase our

knowledge of the interactions present, and to optimise co-crystal prediction programs in the future.

Here we report on the EDD of these weak interactions present in individual crystals of piroxicam (**1**) and saccharin (**2**), and a comparison between a piroxicam–saccharin co-crystal (**3**), in which the asymmetric unit contains one zwitterionic piroxicam and one saccharin molecule. Analysis of the intermolecular bond energies is also presented in an effort to classify key interactions specific to this co-crystal system.

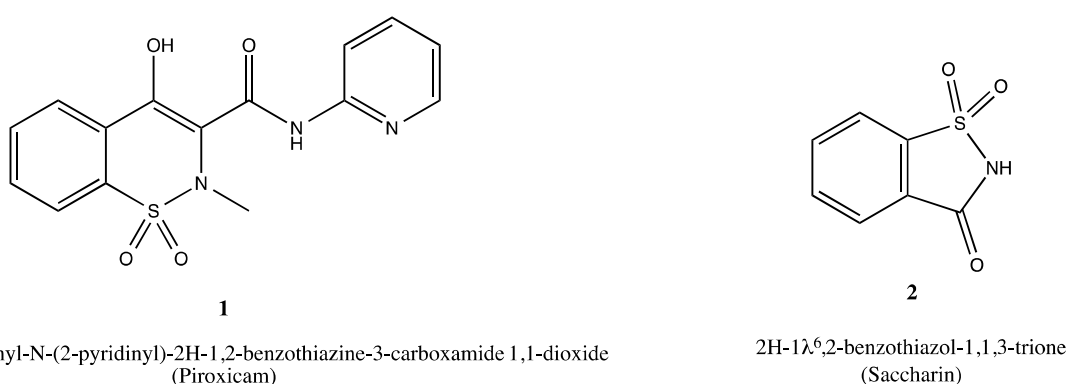


Figure 1 Structures of Piroxicam (**1**) and Saccharin (**2**).

Previous studies, including those of a crystallographic nature, have previously been carried out on complexes 1,([3](#), [11](#)) 2([12](#)) and 3,([13](#)) but none has involved EDD studies. It is believed that the latter will provide further information on the interactions which consistently form in the presence of particular functional groups *i.e.* supramolecular synthons.([14](#), [15](#)) Specifically, these interactions play a key role in the formation and stabilisation of co-crystal systems *via* molecular recognition,([16](#)) and also aid in the engineering and development of more efficacious and non-toxic therapeutics.

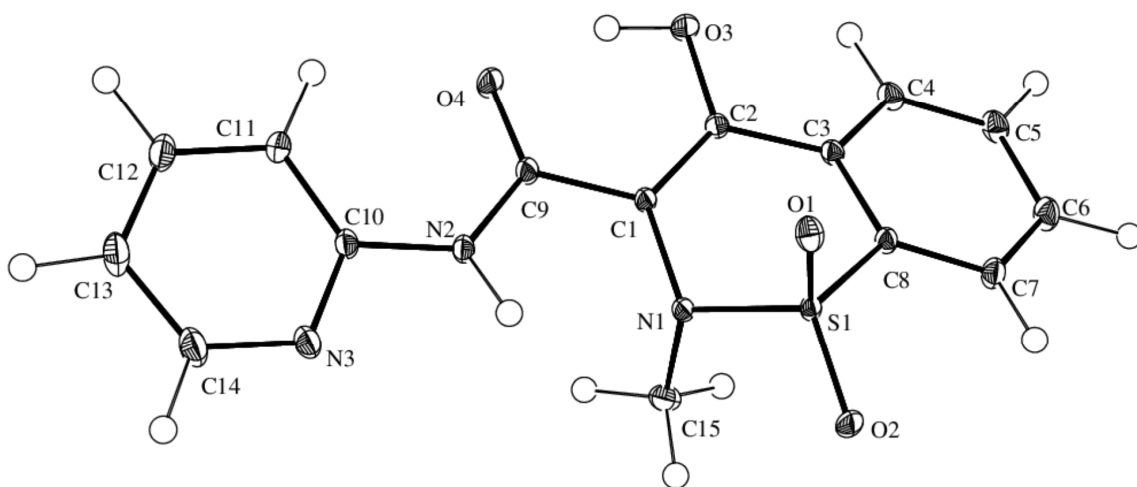


Figure 2: ORTEP diagram of piroxicam (**1**). Thermal ellipsoids are shown at 50% probability level([17](#)).

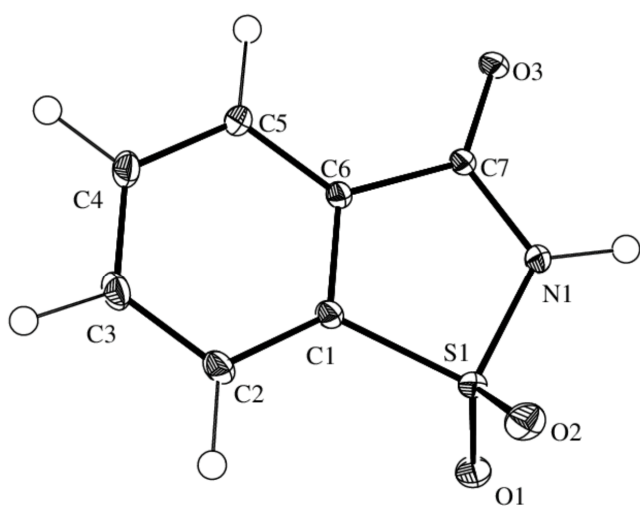


Figure 3: ORTEP diagram of saccharin (**2**). Thermal ellipsoids are shown at 50% probability level([17](#)).

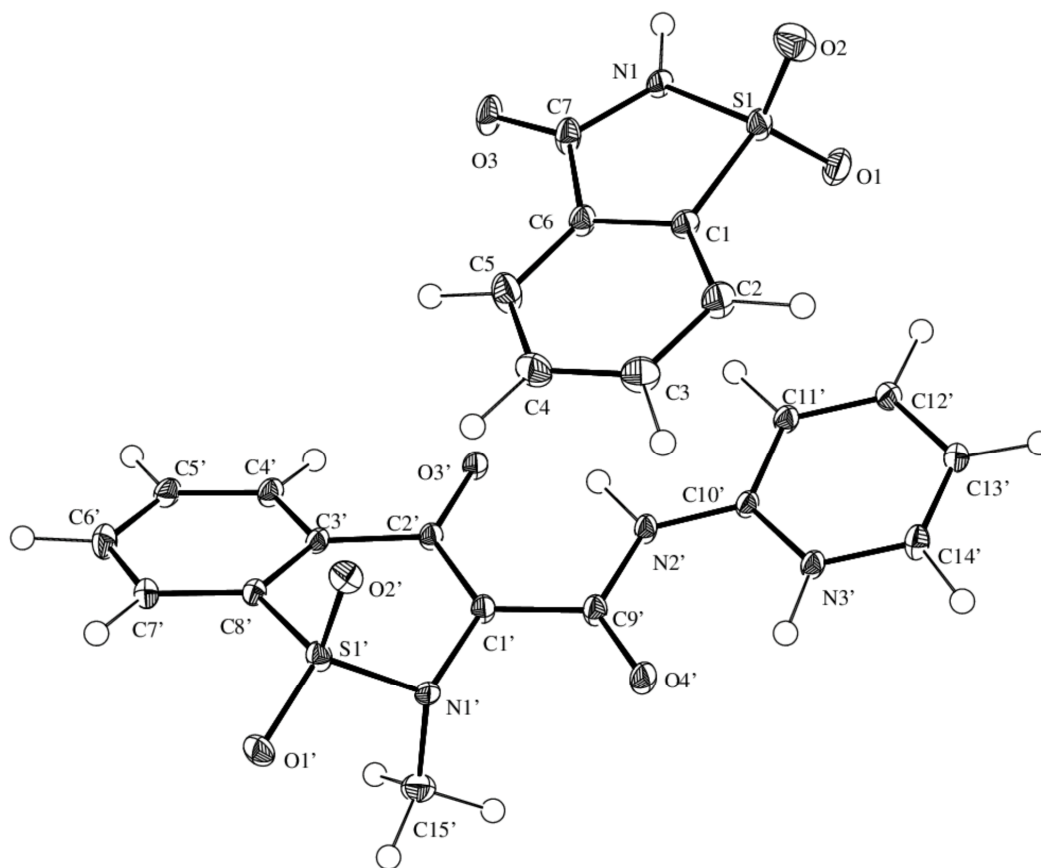


Figure 4: ORTEP diagram of the piroxicam-saccharin co-crystal (**3**). Thermal ellipsoids are shown at 50% probability level([17](#)).

## Methods

### Crystal preparation

Compounds purchased from Sigma-Aldrich and used without further purification. Crystals (**1**) and (**2**) were obtained *via* slow evaporation from acetone. Crystals of (**3**) were obtained following the method described by Banerjee *et al* ([3](#)), from a mixture of equimolar amounts of (**1**) and (**2**) dissolved in a 1:1 mixture of CHCl<sub>3</sub> : MeOH, which was slowly evaporated.

### Data Collection, Integration and Reduction

Single-crystal X-ray diffraction experiments were carried out in the Faculty of Pharmacy at



the University of Sydney using an Agilent SuperNova™ X-ray diffractometer with an X-ray wavelength of 0.7107 Å (MoK $\alpha$ ) at 100K. Crystals of **(1)**, **(2)** and **(3)** with dimensions (0.30 x 0.20 x 0.20) mm, (0.25 x 0.25 x 0.20) mm and (0.25 x 0.20 x 0.20) mm, respectively, were mounted on thin glass fibres with Paratone-N oil being used as both adhesive and cryoprotectant. Data were collected for all crystals using 1°  $\omega$  scans maintaining the crystal-to-detector distance at 5.2 cm for **(1)** and 5.3 cm for **(2)** and **(3)**. For **(1)** and **(2)**, reciprocal space coverage was achieved during the data collection by positioning the detector arm at two different angles in  $2\theta$ , 41.5° and 90.5°. Exposure times of 6 and 24 seconds were used for **(1)**, 20 and 65 seconds for **(2)** respectively. Reciprocal space was covered in **(3)** *via* positioning the detector arm at 41.5° and 72° in  $2\theta$ , with exposure times of 8 and 45 seconds per frame, respectively. A total of 7695, 4652, and 2948 frames were collected for **(1)**, **(2)** and **(3)** respectively.

Integration and reduction of the collected data were performed with the CrysAlis<sup>Pro</sup> software package.<sup>(18)</sup> All crystals were cooled to 100K with an Oxford Cryosystems COBRA cooler. The unit cell parameters for **(1)** were refined from 25496 reflections in the monoclinic space group  $P2_1/c$  with  $Z = 4$ ,  $F(000) = 532$  and  $\mu = 0.303 \text{ mm}^{-1}$ . The unit cell parameters for **(2)** were refined from 13073 reflections in the monoclinic space group  $P2_1/c$  with  $Z = 4$ ,  $F(000) = 376$  and  $\mu = 0.248 \text{ mm}^{-1}$ . The unit cell parameters for co-crystal **(3)** were refined from 35677 reflections in the triclinic space group  $P\bar{1}$  with  $Z$ ,  $F(000) = 688$  and  $\mu = 0.394 \text{ mm}^{-1}$ . Refer to Table 1 for selected crystallographic information from the independent atom model (IAM) and multipole (EXP and SH\_D) refinements.

	<b>1</b>	<b>2</b>	<b>3</b>
Formula	C <sub>15</sub> H <sub>13</sub> N <sub>3</sub> O <sub>4</sub> S	C <sub>7</sub> H <sub>5</sub> NO <sub>3</sub> S	C <sub>22</sub> H <sub>18</sub> N <sub>4</sub> O <sub>7</sub> S <sub>2</sub>
Molecular Mass	331.34	183.18	514.52
Crystal size (mm)	0.25 x 0.20 x 0.20	0.30 x 0.25 x 0.20	0.25 x 0.25 x 0.20
Temperature (K)	100	100	100

Crystal system	Monoclinic	Monoclinic	Triclinic
Space group	$P2_1/c$	$P2_1/c$	$P\bar{1}$
$a$ (Å)	7.034(1)	9.445(1)	9.513(1)
$b$ (Å)	14.989(1)	6.922(1)	10.393(1)
$c$ (Å)	13.894(1)	11.686(1)	12.666(1)
$\alpha$ (°)	90	90	66.968(1)
$\beta$ (°)	96.38(1)	103.06(1)	71.02(1)
$\gamma$ (°)	90	90	89.369(1)
Volume (Å <sup>3</sup> )	1455.90(1)	744.30 (1)	1079.93(2)
$Z$	4	4	2
Refinement Method	Full-matrix least squares on $F^2$	Full-matrix least squares on $F^2$	Full-matrix least squares on $F^2$
No. of reflections collected	198191	170313	298222
No. unique	16911	8965	33446
$R_{\text{int}}$	0.045	0.029	0.038
Completeness (%)	95.8	99.8	94.6
No. reflections used	14742	7800	35677
$\rho_c$ (g cm <sup>-3</sup> )	1.512	1.635	1.582
$F(000)$	688	376	532
$\mu$ (mm <sup>-1</sup> )	0.248	0.394	0.303
$\sin \theta/\lambda_{\text{max}}$	1.11 Å <sup>-1</sup>	1.11 Å <sup>-1</sup>	1.28 Å <sup>-1</sup>
$\theta$ range for data collection (°)	2.718 to 65.67	3.445-65.623	2.920 to 65.651
Index ranges	-17 ≤ $h$ ≤ 18 -38 ≤ $k$ ≤ 38 -34 ≤ $l$ ≤ 35	-23 ≤ $h$ ≤ 24 -17 ≤ $k$ ≤ 17 -29 ≤ $l$ ≤ 29	-24 ≤ $h$ ≤ 24 -24 ≤ $k$ ≤ 24 -32 ≤ $l$ ≤ 32
<u>IAM Refinement</u>			
Final $R1, wR2$	0.034, 0.097	0.022, 0.072	0.038, 0.115
Goodness of fit	1.045	1.094	1.113
Residual density (e Å <sup>-3</sup> )	-0.739, 0.829	-0.437, 0.623	-0.600, 0.510
<u>Multipole Refinement</u>			
$N_{\text{obs}}/N_{\text{var}}$			
<i>Exp</i>	24.1	24.3	29.7
<i>Shade</i>	24.3	24.3	29.7
$R(F), R(F^2)$ , all data			
<i>ExpShade</i>	0.021, 0.031 0.031, 0.032	0.0150, 0.024 0.0150, 0.024	0.024, 0.024 0.0250, 0.0250
$R_w(F), R_w(F^2) > 2\sigma(F)$			
<i>Exp</i>	0.023, 0.045	0.011, 0.022	0.017, 0.033
<i>Shade</i>	0.026, 0.050	0.011, 0.022	0.018, 0.033
Goodness of fit			

<i>Exp Shade</i>	1.707	3.058	2.520
	1.696	3.063	2.536
Residual density (e Å <sup>-3</sup> )			
<i>Exp</i>	-0.25 to 0.27	-0.26 to 0.17	-0.11 to 0.10
<i>Shade</i>	-0.32 to 0.28	-0.27 to 0.19	-0.11 to 0.11

Table 1: Selected Crystallographic Information for complexes **(1)** (piroxicam), **(2)** (saccharin) and **(3)** (piroxicam-saccharin co-crystal).

## Experimental

### Data reduction and refinement strategies

The structures of (1), (2) and (3) were solved using direct methods (SHELXS-2014).(19) In each case, a full-matrix least-squares refinement based on  $F^2$  was performed using SHELXL-2014.(19) The bond lengths between non-hydrogen atoms to hydrogen atoms (X-H bonds, where X=C, O, N) were fixed at average values obtained from neutron diffraction studies, taken from Allen *et al.*,(20) O-H, N-H, and C-H bond lengths being 0.967, 1.009, and 1.083 Å respectively, with bond vectors taken from the original riding H-atom models in the IAM refinement. All non-hydrogen atoms were refined anisotropically.

The coordinates and anisotropic temperature factors from the IAM were then imported into XD,(21) a program that uses a least-squares procedure to refine a rigid pseudo-atom model in the form of the Hansen-Coppens multipole formalism.(22) In this formalism, the electron density,  $\rho(\mathbf{r})$  within a crystal is described by the summation of aspherical pseudoatoms (each with its own electron density) with nuclear positions  $\mathbf{r}_j$  as shown in the Equation (1).

$$\rho(\mathbf{r}) = \sum_j \rho_j(\mathbf{r} - \mathbf{R}_j) \quad (1)$$

The complete density of the pseudo-atomic model is modelled by Equation (2).

$$\rho_j(\mathbf{r}_j) = P_c \rho_c + \kappa' {}^3P_v \rho_v(\kappa' r) + \kappa' {}''^3 \sum_{l=0}^{l_{\max}} \sum_{m=-1}^{m=1} P_{lm} R_l(\kappa' r_j) d_{lmj}(\theta_j, \Phi_j) \quad (2)$$

The expression for the pseudo-atom density includes the usual spherical core, a term to describe the spherical component of the valence density, plus a deformation term describing the asphericity of the valence density. The radial functions  $\{R_l(r_j)\}$  are modulated by angular functions  $\{d_{lmj}(\theta_j, \Phi_j)\}$  defined by axes centred on each atom. A number of radial functions may be used, the most common being Slater-type functions given in Equation (3).

$$R_l(r) = Nr^{n_l} \exp(-\zeta_l r) \quad (3)$$

The multipole refinement process began with an analysis of the results of higher order spherical atom refinement (usually  $\sin \theta/\lambda > 0.7 \text{ \AA}^{-1}$ ), providing accurate atomic positions and temperature factors forming the basis for the remainder of the refinement.

It has been shown that third row atoms are often inadequately modelled by the standard  $n_l$ -set of (4,4,4,4,4), mainly due to the fact that these were originally modelled using node-less single-zeta functions to model the valence density. The coefficients  $n_l$  are chosen so that the maximum of the radial function is at the peak density position for each shell. We and others have previously shown that this standard description is particularly troublesome for sulfur(23-25) and usually results in high residual electron density in the proximity of the sulfur atoms at the completion of the refinement. To address this issue we adopted a model where the  $n_l$ -set for sulfur used in this work was (4,4,4,5,5)(26). Additionally, optimisation of the sulfur core electron density distribution was introduced by assigning a spherical expansion/contraction coefficient ( $\kappa'$ ), to the 1s, 2s and 2p electrons, which was allowed to refine. The value of  $\zeta$  for sulfur was that of the free atom ( $7.278 \text{ \AA}^{-1}$ )(27).

The refinement was performed by introducing the multipole expansion in a stepwise manner, ultimately being truncated at the octapole level ( $l_{max} = 3$ ) for C, O, N and S. Each C, O, N and S atom was assigned a kappa prime ( $\kappa'$ , a spherical function which governs 3D directional expansion/contraction of the valence shell) during the refinement to allow for accurate modelling of electron density, and finally a  $\kappa''$  value, which models radial expansion/contraction of the valence electrons. The density of hydrogen atoms was modelled using a single monopole, with  $\kappa'$  fixed at 1.2, with the aspherical density modelled by a single bond-directed dipole ( $l_{max} = 1$ ). The refinements were continued until convergence was reached for each multipole before the next one was introduced. The Hirshfeld rigid bond test

was used to determine if the anisotropic displacement parameters were of any actual physical significance; *i.e.*, the electron density was successfully deconvoluted from the inherent thermal smearing.(28) This test measures the differences in mean-squared displacement amplitudes (DMSDA) with ADPs deemed to be described as physically meaningful if they are below  $1 \times 10^{-3} \text{ \AA}^2$ . The average value obtained from these refinements is  $4 \times 10^{-4} \text{ \AA}^2$ . Scale and temperature factors were refined separately from the multipole models described above, except in the final refinement cycles, where the full variance-covariance matrix is needed in order to get meaningful standard uncertainties (su). In all cases, reflections were required to have an intensity of  $F > 3\sigma(F)$  in order to be included in the refinement. This model is termed EXP in the remainder of the manuscript.

### **Anisotropic Temperature Refinement of Hydrogen Atoms**

An alternative multipole refinement was carried out using anisotropic temperature factors for the hydrogen atoms as well as the heavy atoms, as discussed by Hoser *et al.*(29) regarding the increased accuracy of the multipole model obtained from multipole refinement involving the use of anisotropic temperature factors for hydrogen.(29, 30) Anisotropic temperature factors for the hydrogen atoms were calculated using the SHADE3 server developed by Madsen.(31) Multipole analyses with anisotropic temperature factors for hydrogen were truncated at the same level as above ( $l_{\text{max}} = 3$ ) for heavy atoms and up to the ( $l_{\text{max}} = 1$ ) for hydrogen atoms). The multipole refinement for hydrogen atoms was stopped at the dipolar expansion as the observations reported by Nguyen *et al.*(9) illustrated that refinement of hydrogen atoms in the multipole model past the dipolar to the quadrupolar level was generally unnecessary and would not lead to improved modelling of the electron density. However, it should be noted that the decision to refine hydrogen atoms anisotropically should be made on a per case basis.

Refer to Table S1 in supplementary data for the anisotropic displacement parameters used. This model is termed *Shade* in the remainder of this manuscript.

## Computational Methods

Gas phase, single point (SP) calculations were performed on **(1)**, with the geometry taken from the high-order experimental coordinates. Geometry optimisation (OPT) as well as SP calculations were also performed on all structures. All theoretical calculations were performed with the Gaussian 09 suite([32](#)) at the 6-31+G(d,p) level of theory for all structures. All calculations used the three-parameter hybrid exchange function developed by Becke([33](#)) in conjunction (*vide supra*) with the exchange correlation potential, corrected *via* gradient developed by Lee *et al.*([34](#)) (B3LYP). Analysis of the topology of electron density from the experimental model was performed using the XDPROP portion of XD,[\(21\)](#) while analysis of the electron density for the theoretical densities was performed using the AIMALL([35](#)) package.

## Results and Discussion

### Geometry

Bond lengths and angles for all experimental structures were obtained from the multipole model (MM) refinement output, while bond lengths for the theoretical structures were obtained from DFT optimisation.<sup>(32)</sup> For **(1)**, the X-ray structure was in excellent agreement with results reported by Koji-Prodic *et al.*<sup>(36)</sup> in 1982, and also correlate well with the optimised geometry model (OPT), with mean differences of 0.006 Å and 0.4° for bond lengths and angles, respectively. A similar situation was also seen for **(2)**, where the geometrical details obtained from IAM refinement were in good agreement with the bond lengths and angles reported by Bart in 1968<sup>(13)</sup> with mean differences of 0.008 Å for bond length and 0.01° for angles, respectively. Comparison between the MM structure and DFT optimisation of **(2)** revealed that bond lengths and angles differed by an average of 0.010 Å and 0.05°, respectively. For complex **(3)**, our data are in good agreement with values reported by Bhatt *et al.* in 2005<sup>(37)</sup> with mean differences of only 0.008 Å for bond lengths and 0.06° for angles. Interestingly, **(3)** is made up of a single molecule of saccharin, and a zwitterionic piroxicam, where the hydroxyl hydrogen (H3A) from O(3) is now found on the pyridyl nitrogen atom N(3). This has the effect of rotating the pyridyl group approximately 180° around the N(2) – C(10) bond compared to **(1)**, and forms an intramolecular hydrogen bond with the amide oxygen atom O(4). Refer to Tables S2 – S5 in supplementary data for a comparison of experimental and theoretical bond lengths and angles.

### Sulfur core optimisation



As outlined above, it was necessary to optimise the standard description of sulfur in this refinement. Each sulfur atom (in each compound) was split so that the core shells ( $1s^2$ ,  $2s^2$ ,  $2p^6$ ) has a spherical expansion/contraction coefficient ( $\kappa$ ) and a fixed population, while the valence shell ( $3s^2$ ,  $3p^4$ ) had both spherical and aspherical  $\kappa$  values, as well as population refined. The suitability of this model is demonstrated in Table 2, where maximum and minimum residual errors are significantly smaller in most cases than those obtained from the standard model for sulfur. This is most evident in **3**, where residuals of as much as  $-0.41$  and  $+0.32 \text{ e } \text{\AA}^{-3}$  are reduced to  $-0.11$  and  $0.10 \text{ e } \text{\AA}^{-3}$ , where all such peaks and troughs are located within  $1 \text{ \AA}$  from S nuclei.

Table 2 details the results of the refined  $\kappa$  values for the sulfur atoms in all three structures, along with the associated monopole populations. For **(1)**, in a standard MM refinement, both the spherical and aspherical components of the valence density are expanded, when compared to that of the free atom. However, when a core optimised approach is taken, the radial behaviour of the valence density changes and is essentially equal to that of the free atom. Interestingly, in **(2)**, the situation is somewhat different, despite the similar chemical environment of the sulfonyl group. Here the valence density is contracted, as is the aspherical component, when compared to the free atom. For **(3)**, the situation is similar to that in **(1)**, with spherical components of both core and valence electron density expanded, while the aspherical density is slightly expanded. We note that  $\kappa$  in the standard refinement settles at a very unrealistic value of 1.6. For the core optimised refinement, the valence population of sulfur is maintained across **(1)** and both molecules in **(3)** at an average of  $5.6 \text{ e}$ , whereas the same atom in **(2)** having a population that surprisingly differs by approximately  $1 \text{ e}$  at  $4.7 \text{ e}$ .

Atom Label	Kappa'	Kappa''	Population (e)	R(F)	Max/Min
------------	--------	---------	----------------	------	---------

					<b>Residual</b>
					$e \text{ \AA}^{-3}$
<b>Piroxicam (1)</b>					
S(1) <sub>valence</sub>	0.9498	1.0002	5.8561		
S(1') <sub>core</sub>	0.9846	1.0000	10.0000	0.0219	0.27/-0.25
	(0.9876)	(0.9746)	(5.7451)	(0.0217)	(0.34/-0.37)
<b>Saccharin (2)</b>					
S(1) <sub>valence</sub>	1.0539	1.0119	4.7348		
S(1') <sub>core</sub>	1.0300	1.0000	10.0000	0.015	0.27/-0.25
	(1.0447)	(0.9629)	(4.5679)	(0.015)	(0.26/-0.35)
<b>Co-crystal (3)</b>					
<b>Piroxicam</b>					
S(1'A) <sub>valence</sub>	0.9751	1.0649	5.5666		
S(1'B) <sub>core</sub>	0.9414	1.0000	10.0000	0.021	0.10/-0.11
	(1.0437)	(1.6286)	(4.7051)	(0.027)	(0.32/-0.41)
<b>Saccharin</b>					
S(1A) <sub>valence</sub>	0.9751	1.0649	5.5438		
S(1B) <sub>core</sub>	0.9414	1.0000	10.0000		
	-	-	(4.5193)		

Table 2 – Expansion/contraction coefficients (kappas) for sulfur. Values in parentheses refer to a standard un-optimised (4,4,4,4,4) refinement.

### Isotropic vs. Anisotropic Refinement of Hydrogen Atoms

The temperature factors of hydrogen atoms were anisotropically modelled based upon discussions by Hoser *et al.*,<sup>(29)</sup> Spackman *et al.*<sup>(38-40)</sup> and Koritsansky *et al.*<sup>(41)</sup> These studies have observed dissimilarities in the topological analysis of weak interactions such as H-bonds, van der Waals forces and  $\pi$ - $\pi$  stacking interactions.<sup>(30)</sup> To observe the effect of applying calculated anisotropic temperature factors for hydrogen atoms during multipole

refinement, anisotropic temperature factors were calculated(31) and the resulting ADPs transferred to the multipole model. Hirshfield's rigid bond test was applied and the mean DMSDA values for the *Exp* refinement were  $1.21 \times 10^{-4}$ ,  $1.56 \times 10^{-4}$  and  $1.85 \times 10^{-4} \text{ \AA}^2$  for (1), (2) and (3), respectively. Similarly, the DMSDA values for the *Shade* refinement were  $1.20 \times 10^{-4}$ ,  $1.58 \times 10^{-4}$  and  $1.92 \times 10^{-4} \text{ \AA}^2$ . All mean DMSDA values are below  $1 \times 10^{-3} \text{ \AA}^2$ , indicating that the ADPs (including hydrogen atoms) employed in the multipole refinements had sufficiently accounted for the thermal motion of the atoms. As shown in the graphs in the supplementary material (Figures Sx-y), *Exp* and *Shade* refinements show generally good agreement across most of the H-bonds. The main differences between *Exp* and *Shade* analyses were seen in the weak ( $E_{\text{HB}} < 20 \text{ kJ mol}^{-1}$ ) or strong H-bonds ( $E_{\text{HB}} > 60 \text{ kJ mol}^{-1}$ ), and bonds with intermediate energy values being essentially identical. Both observations are in accordance with those reported by Nguyen *et al.*(9) Our findings show that the use of anisotropic temperature factors in hydrogen atom refinement provides no significant difference in topology, (both intra- and intermolecular); and the application of ADPs to hydrogen atoms is deemed unnecessary in this case; thus the discussion will focus on the isotropic hydrogen atom model.

## Topological Analysis

Topological analysis of both the theoretical and experimental structures density was carried out and completeness of the analysis was ensured through satisfaction of the Poincaré-Hopf or its crystalline equivalent Morse relationship.(42) Intramolecular BCPs corresponding to all expected covalent bonds are found in the analysis of all complexes: refer to Supplementary Data Table S6-7 for details of the full topological analysis. There is generally a good correlation between  $\rho_{\text{bcp}}$  and  $\nabla^2\rho_{\text{bcp}}$  values obtained from the *Exp* and SP densities for all

complexes, shown through the small differences in  $\rho_{\text{bcp}}$  and  $\nabla^2\rho_{\text{bcp}}$ . For **(1)** and **(2)**, in non- S-O bonds, average differences of -0.05 and -0.02 e  $\text{\AA}^{-3}$  and 3.52 and -1.32 e  $\text{\AA}^{-3}$  were seen for  $\rho_{\text{bcp}}$  and  $\nabla^2\rho_{\text{bcp}}$ , respectively. For **(3)**, there was a mean difference for non- S-O bonds of 0.07 and 0.59 e  $\text{\AA}^{-3}$  for  $\rho_{\text{bcp}}$  and  $\nabla^2\rho_{\text{bcp}}$  between experiment and theory. Laplacian plots for **(1)**, **(2)** and **(3)** are shown below (Figures 5 a,- f).

In the S–O bonds, however, agreement between experiment and theory is poor (Table 3). For **(1)** the largest differences seen are in the topology of the sulfonyl bonds; DFT underestimates  $\rho_{\text{bcp}}$  by 0.34 e  $\text{\AA}^{-3}$  in S(1) – O(1), and overestimates this quantity in S(1) – O(2) by 0.1 e  $\text{\AA}^{-3}$ . Even larger differences in  $\nabla^2\rho_{\text{bcp}}$  are found, where DFT overestimates this value by between 12 and 27 e  $\text{\AA}^{-3}$ . For **(2)**, the effect on the Laplacian sulfonyl bonds is far more pronounced, and differences in  $\nabla^2\rho_{\text{bcp}}$  values between experiment and DFT for the S=O bonds were as much as 40 e  $\text{\AA}^{-3}$ . In **(3)**, the maximum difference is again seen in the S1'-O2' bond, for which a discrepancy of 30 e  $\text{\AA}^{-3}$  is seen in  $\nabla^2\rho_{\text{bcp}}$ . The large discrepancies here may be attributed to the inability of the experimental model to properly account for the valence electrons of heavy atoms such as sulfur, further compounded by the proximity of two oxygen atoms which may also contribute to a large amount of unaccounted for electrons.

	$\rho$ (e $\text{\AA}^{-3}$ )			$\nabla^2\rho$ (e $\text{\AA}^{-5}$ )			$\epsilon$		
	EXP	SH_D	SP	EXP	SH_D	SP	EXP	SH_D	SP
<b>Piroxicam (1)</b>									
<b>S(1) - O(1)</b>	2.39	2.38	2.05	1.48	1.65	28.93	0.17	0.16	0.01
<b>S(1) - O(2)</b>	1.96	1.96	2.05	15.86	15.99	29.77	0.21	0.20	0.03
<b>Saccharin (2)</b>									
<b>S(1) - O(1)</b>	2.26	2.26	2.01	-5.47	-5.25	32.42	0.08	0.08	0.07
<b>S(1) - O(2)</b>	2.27	2.27	2.01	-7.71	-7.48	32.65	0.06	0.06	0.07

<b>Piroxicam (3)</b>									
	-								
<b>S(1') - O(1')</b>	2.31	2.29	2.00	-7.75	-6.37	32.24	0.07	0.07	0.03
<b>S(1') - O(2')</b>	2.31	2.20	1.98	-0.62	0.12	32.14	0.19	0.19	0.01
<b>Saccharin (3)</b>									
<b>S(1) - O(1)</b>	1.90	1.88		25.44	26.86	32.82	0.38	0.37	0.07
<b>S(1) - O(2)</b>	2.38	2.37		-10.38	-9.85	32.13	0.09	0.10	0.07

Table 3: Sulfur – Oxygen topology in **(1)**, **(2)** and **(3)**.

DFT universally predicts large, positive values of  $\nabla^2\rho_{\text{bcp}}$ , indicative of closed-shell interactions, whereas experiment finds no such fixed pattern. However, interpretation of such values has been shown to be complicated by the rapidly changing nature of  $\nabla^2\rho$  in such polar covalent bonds, where the BCP is often located close to the point where  $\nabla^2\rho$  changes sign. As shown in Figure 5, Laplacian diagrams for S=O bonds in each of the complexes show a clear overlap of the valence shell charge concentration, resulting in what appears to be open shell interactions, albeit with a severe pinching off in the S(1) O(2) bond in saccharin. These discrepancies are commonly seen in polar bonds such as these, and can be explained by the experimental density changing more quickly than the theoretical counterpart(43). This phenomenon is also seen when the electron density and Laplacian of the S=O bonds are plotted against bond length. It can be seen that the electron density for both EXP and DFT follow a similar pattern, however a different story is seen in the Laplacian, with the EXP showing significant closed shell interactions as seen through the highly negative values of the Laplacian in the EXP model. In contrast, the DFT models graphed along the same axes show significantly less negative Laplacian highlighting an open shell interaction more indicative of covalent bonding. Complete graphs of the electron density and Laplacian can be found in Supplementary Information Figure S1-2.

Thus, very small differences in the total electron density, of the same magnitude as the residual errors stemming from the multipole model, are amplified in the Laplacian into apparently major discrepancies between experiment and theory(23, 24, 43). It should be noted here that there is no appreciable difference between the *Exp* and the *Shade* refinements, across all datasets the maximum differences are  $0.30\text{e}\text{\AA}^{-3}$  for  $\rho_{\text{bcp}}$  and  $-1.5\text{e}\text{\AA}^{-5}$  in  $\nabla^2\rho_{\text{bcp}}$ .

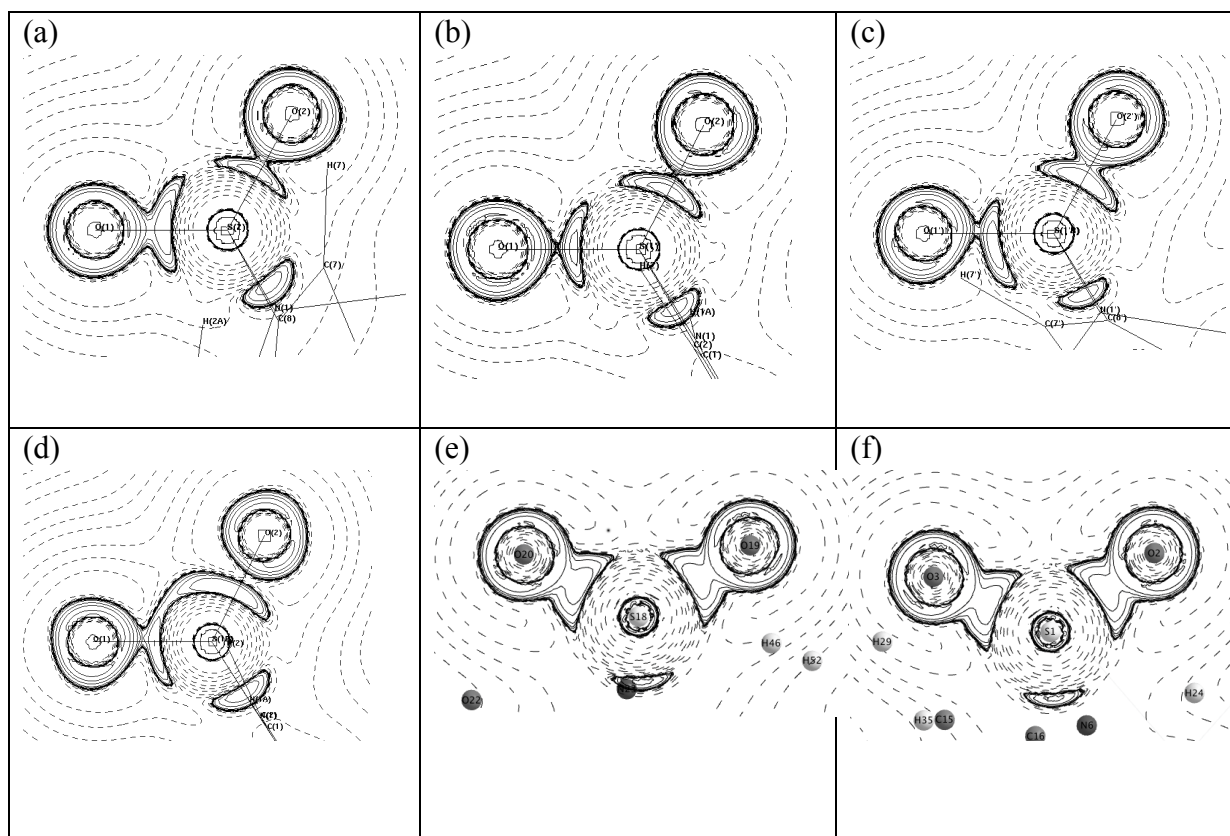


**Figure 5:** *Exp* -  $\nabla^2\rho_{\text{bcp}}$  distribution of the O(1) – S(1) – O(2) plane for piroxicam in (a) **(1)**, (b) **(2)**, (c) **(3)**, (d) saccharin in **(3)**, and (e) theoretical for piroxicam in **(3)**, and (f) saccharin in **(3)**. The theoretical Laplacian plots of individual molecules in **(1)** and **(2)** show no appreciable differences from plots in (e) and (f) and are thus not shown.

As well as considering agreement with DFT, Table 3 shows that even within a single molecule there are significant differences between S-O bonds depending on their environment. Geometrical considerations suggest that **(1)** contains a hydrogen bond from O(2) to a symmetry-related H(2)-N(2) group (N...O = 3.002 Å). **(3)** contains a hydrogen bond from O(2') to symmetry-related H(3')-N(3') (N...O = 3.015 Å), and also from O(2) to

symmetry-related H(3')-N(3') (N...O = 3.048 Å). In contrast, **(2)** contains no hydrogen bonds with S-O groups as H-bond acceptors. Table 3 indicates that **(1)** and **(3)** exhibit marked differences in the topology of S-O bonds, whereas those in **(2)** are almost identical. This leads us to suspect that the effects of the crystalline environment are at least partly responsible for the patterns observed in Table 3, a possibility that is explored in more detail using the EDD below.

## Hydrogen Bonds

A total of 9, 5 and 12 classical hydrogen bonds were found for **(1)**, **(2)** and **(3)**, respectively. Topological details of the corresponding BCPs for are reported in Table 4 with details of the SHADE refinement removed for clarity. The full table can be found in Supplementary Data Table S9, and geometrical details can be found in Supplementary Data Table S8. The bonds found include those with traditional donors and acceptors (such as N – H and O – H to O and N), and also those validated by Koch *et al*([44](#)) of the form C-H...O and C-H... $\pi$  contacts. Analysis of the bonds showed that N-H...C and N-H...O arrangements were the most linear, while the least linear H-bonds are N-H...O, O-H...N and C-H...O bonds. It was also found that C-H...C and C-H...O bonds had the largest distance between the hydrogen and acceptor atoms, while N-H...O bonds had the shortest distance. No notable correlations were found between donor to acceptor lengths for the different types of H-bond, with **(1)** having the longest donor to acceptor length in bonds where the acceptor group was C-H, followed by O-H and N-H donor groups. For **(2)**, a converse pattern was found with N-H groups having the longest donor to acceptor bond length. It should be noted for all of the above cases, that different H-bond lengths, even for those with the same donor and acceptor groups is normal due the crystal field effect, especially in the case of **(1)** where intermolecular H-bonds within

the same asymmetric unit would in most cases be shorter than those which extend to molecules in other asymmetric units or unit cells.

Hydrogen bonds according to Koch *et al.*([44](#)) are characterised by relatively low  $\rho_{\text{bcip}}$  and positive  $\nabla^2\rho_{\text{bcip}}$ . Topological analysis of H-bonds was performed for both the *Exp* and *Shade* models, while intramolecular H-bonds and those in a discrete dimer of the co-crystal from experimental coordinates, were also analysed *via* DFT. For **(1)**, three intramolecular H-bonds were found in both the experimental and theoretical analyses, with a further six intermolecular hydrogen bonds located between neighbouring molecules. For **(3)**, three of the bonds found were considered to be within the asymmetric unit between the piroxicam and saccharin molecules. Figure 6 shows the weak interactions present in the co-crystal **(3)**.

Dissociation energies of the hydrogen bonds were calculated by applying the methods of Abramov ([46](#)) and Espinosa([47](#)); topological parameters such as electron density could be used to estimate the kinetic, potential and total energy densities related to a bond, and hence to estimate the strength of a hydrogen bond. The ratio  $-G/V$  can also be used to estimate covalency in H-bonds: a value of between 0.5 and 1 indicates partly covalent character, while a value of greater than 1 is considered to be purely non-covalent([48](#)). H-bonds can be separated into three groups by their strengths; weak H-bonds ( $E_{\text{HB}} < 20 \text{ kJ mol}^{-1}$ ), moderate strength H-bonds ( $E_{\text{HB}} = 20\text{-}40 \text{ kJ mol}^{-1}$ ) and strong H-bonds ( $E_{\text{HB}} > 60\text{kJ mol}^{-1}$ ). In **(3)**, two intramolecular and one intermolecular contacts are considered to be strong hydrogen bonds, with the remainder considered to be weak H-bonds or  $\pi\cdots\pi$  contacts. Similar trends can be seen in **(1)** and **(2)**, with the majority of the H-bonds being classified as weak (six for **(1)** and four for **(2)**, two of the H-bonds in **(1)** being of moderate strength and the rest in both being considered to be strong.



	$\rho$	$\nabla^2\rho$	$\varepsilon$	$G$	$V$	$H$	$E_{\text{HB}}$
	/ eÅ <sup>-3</sup>	/ eÅ <sup>-5</sup>		/ E <sub>h</sub> eÅ <sup>-3</sup>	/ E <sub>h</sub> eÅ <sup>-3</sup>	/ E <sub>h</sub> eÅ <sup>-3</sup>	/ kJ mol <sup>-1</sup>
<b>Intermolecular</b>							
N(2)-H(2A) ... O(2)	0.073	1.248	0.33	0.07	-0.05	0.02	19.45
C(5) - H(5) ... O(2)	0.049	0.750	0.43	0.04	-0.03	0.01	11.67
C(5) - H(5) ... O(1)	0.045	0.739	0.53	0.04	-0.03	0.01	11.67
C(14) - H(14) ... O(4)	0.012	0.437	2.27	0.02	-0.01	0.01	3.89
C(15) - H(15A) ... O(1)	0.039	0.672	0.09	0.03	-0.02	0.01	7.78
C(15) - H(15B) ... O(1)	0.047	0.743	0.11	0.04	-0.03	0.01	11.67
<b>Intramolecular</b>							
N(2) - H(2A) ... N(1)	0.166	2.185	1.91	0.14	-0.13	0.01	50.57
O(3) - H(3A) ... O(4)	0.362	5.038	0.03	0.38	-0.41	0.01	159.51
C(11) - H(11) ... O(4)	0.119	1.606	0.14	0.10	-0.08	0.01	31.12
<b>Close Contacts</b>							
C(3)...C(12)	0.034	0.313	0.46	0.02	-0.01	0.00	3.89
C(4)...C(10)	0.037	0.359	3.56	0.02	-0.01	0.01	3.89
C(5)...C(9)	0.036	0.343	0.48	0.02	-0.01	0.00	3.89
H(12)...H(6)	0.013	0.599	0.13	0.03	-0.02	0.01	7.78
H(11)...H(15C)	0.024	0.323	0.47	0.02	-0.01	0.01	3.89

**Table 4** Topological analysis of hydrogen bonding in (**1**). Standard uncertainties have been omitted from the table for clarity. They are closely scattered around 0.02 e Å<sup>-3</sup> ( $\rho_{\text{bcp}}$ ) and 0.05 e Å<sup>-5</sup> ( $\nabla^2\rho_{\text{bcp}}$ ).

	$\rho$	$\nabla^2\rho$	$\varepsilon$	$G$	$V$	$H$	$E_{\text{HB}}$
	/ eÅ <sup>-3</sup>	/ eÅ <sup>-5</sup>		/ E <sub>h</sub> eÅ <sup>-3</sup>	/ E <sub>h</sub> eÅ <sup>-3</sup>	/ E <sub>h</sub> eÅ <sup>-3</sup>	/ kJ mol <sup>-1</sup>
<b>Intermolecular</b>							
N(1)-H(1A) ... O(3)	0.20	3.61	0.00	0.23	-0.20	0.03	77.81
C(2) - H(2) ... O(2)	0.04	1.00	0.42	0.05	-0.03	0.02	11.67
C(3) - H(3) ... O(2)	0.05	0.65	0.04	0.04	-0.03	0.01	11.67
C(4) - H(4) ... O(1)	0.05	0.73	0.14	0.04	-0.03	0.01	11.67
C(5) - H(5) ... O(3)	0.07	0.96	0.03	0.05	-0.04	0.01	15.56
<b>Close Contacts</b>							
C(7) ... C(5)	0.03	0.33	1.49	0.02	-0.01	0.00	3.89
O(1) ... C(7)	0.04	0.46	1.06	0.03	-0.02	0.01	7.78
O(1) ... C(6)	0.04	0.46	1.06	0.03	-0.02	0.01	7.78

**Table 5** Topological analysis of hydrogen bonding in (2). Standard uncertainties have been omitted from the table for clarity. They are closely scattered around 0.02 e Å<sup>-3</sup> ( $\rho_{\text{bcp}}$ ) and 0.05 e Å<sup>-5</sup> ( $\nabla^2\rho_{\text{bcp}}$ ).

	$\rho$	$\nabla^2\rho$	$\varepsilon$	$G$	$V$	$H$	$E_{\text{HB}}$
	/ eÅ <sup>-3</sup>	/ eÅ <sup>-5</sup>		/ E <sub>h</sub> eÅ <sup>-3</sup>	/ E <sub>h</sub> eÅ <sup>-3</sup>	/ E <sub>h</sub> eÅ <sup>-3</sup>	/ kJ mol <sup>-1</sup>
<b>Intermolecular</b>							
N(1)-H(1A) ... O(3')	0.32	4.23	0.05	0.32	-0.34	-0.02	132.28
N(3') - H(3A') ... O(2')	0.07	0.89	0.32	0.05	-0.04	0.01	15.56
C(3) - H(3) ... O(4')	0.05	0.72	0.35	0.04	-0.03	0.01	11.67
C(3) - H(3) ... N(1')	0.03	0.77	1.04	0.04	-0.02	0.02	7.78
C(4) - H(4) ... O(2')	0.06	0.88	0.06	0.05	-0.03	0.01	11.67
C(5') - H(5') ... O(2)	0.04	0.90	0.46	0.05	-0.03	0.02	11.67
C(11') - H(11') ... O(3)	0.05	1.29	0.29	0.07	-0.04	0.02	15.56
C(12') - H(12') ... O(1)	0.06	0.67	0.08	0.04	-0.03	0.01	11.67

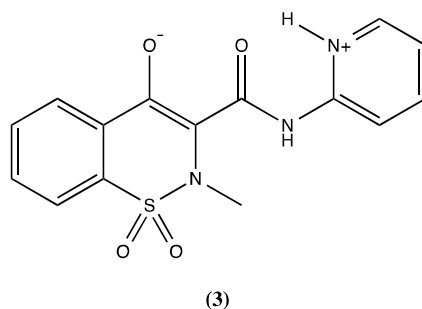
<b>C(14') - H(14') ... O(2)</b>	0.04	0.52	0.33	0.03	-0.02	0.01	7.78
<b>C(15') - H(15C) ... O(3)</b>	0.05	0.84	0.11	0.04	-0.03	0.01	11.67
Intramolecular							
<b>N(2') - H(2A') ... O(3')</b>	0.29	3.94	0.04	0.29	-0.30	-0.01	116.71
DFT							
<b>N(3') - H(3A') ... O(4')</b>	0.23	3.07	0.17	0.21	-0.21	0.00	81.70
DFT							
Close Contacts							
<b>C(1') ... C(4) - <math>\pi</math> ... <math>\pi</math></b>	0.03	0.30	0.39	0.02	-0.01	0.00	3.89
<b>C(2') ... C(11') - <math>\pi</math> ... <math>\pi</math></b>	0.04	0.34	0.22	0.02	-0.02	0.00	7.78
<b>C(4') ... C(13') - <math>\pi</math> ... <math>\pi</math></b>	0.04	0.36	0.35	0.02	-0.02	0.00	7.78
<b>C(4) ... N(2')</b>	0.03	0.31	1.09	0.02	-0.01	0.00	3.89
<b>C(5) ... O(3') - <math>\pi</math> ... C=O</b>	0.03	0.34	0.83	0.02	-0.01	0.01	3.89
<b>C(6') ... H(15B)</b>	0.04	0.41	0.74	0.02	-0.02	0.01	7.78
<b>C(7') ... H(15B)</b>	0.04	0.41	0.74	0.02	-0.02	0.01	7.78
<b>C(11') ... C(2)</b>	0.03	0.31	1.63	0.02	-0.01	0.00	3.89
<b>C(7) ... C(7)</b>	0.06	0.70	3.18	0.04	-0.03	0.01	11.67
<b>C(7) ... O(3) - C=O</b>	0.06	0.70	3.18	0.04	-0.03	0.01	11.67
<b>H(4') ... H(1A)</b>	0.03	0.34	0.83	0.02	-0.01	0.01	3.89

**Table 6** Topological analysis of hydrogen bonding in **(3)**. Standard uncertainties have been omitted from the table for clarity. They are closely scattered around  $0.02 \text{ e } \text{\AA}^{-3}$  ( $\rho_{\text{bcp}}$ ) and  $0.05 \text{ e } \text{\AA}^{-5}$  ( $\nabla^2\rho_{\text{bcp}}$ ).

### Atomic Charges

As mentioned previously, in **(3)** the piroxicam moiety is found as the zwitterion (Figure 8), such that nature of the ionisation/charge on the oxygen and nitrogen and associated functional groups should be seen in the charge distribution. The monopolar electron population (Pv) was determined for each atom in **(1)** and **(2)**, and was compared to each atom in **(3)**. Surprisingly,

the average difference of atomic charges within piroxicam molecules in **(1)** and **(3)** is just 0.004 e, with the greatest difference of +0.28 e seen in H2A, *i.e.*, the hydrogen located on amide nitrogen. For saccharin the average difference between **(2)** and **(3)** was more pronounced, albeit on average very small, with an average of -0.02 e, with the greatest change seen in S(1) of -0.71 e when compared to its counterpart in **(3)**. In both molecules, differences of around 0.2 e were seen consistently across the sulfonyl oxygen atoms, with those in **(3)** being the more negative; this is possibly due to the large number of weak interactions in the co-crystal.

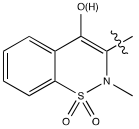
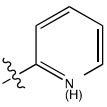
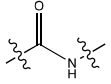


**Figure 8:** Zwitterionic structure of piroxicam in **(3)**.

Somewhat surprisingly, the groups bearing formal positive and negative charges in **(3)** show very small changes from their charges in pure crystalline forms. For the phenolic O(3) – H(3A) group, there was very small change from **(1)** to **(3)**, with H(3A) becoming slightly more negative in **(3)**, by 0.08 e. The pyridyl nitrogen atom N(3), also had an insignificant change in monopolar charge, becoming more negative -0.01 e. The lack of localised monopole charges in zwitterionic compounds has been observed in experimental charge density studies previously,[\(23\)](#) and it is generally found that the changes in charge are ‘delocalised’ across neighbouring atoms.

To examine this phenomena, piroxicam was partitioned into three distinct groups (Table 7), and the combined charges of atoms in each of these groups determined. This data shows that, whether charges are determined from refined monopole values (Pv) or integration over atomic basins ( $\Omega$ ), the change from **(1)** to **(3)** leads to the benzothiazinedioxide fragment (A) becoming substantially more negative and the pyridyl (B) and amide (C) groups becoming positive. Theoretical values, however, do not agree with this pattern, presumably due to the lack of crystalline environment in DFT calculations, and so are omitted from Table 7. Thus, while individual atoms do not reflect the formal charges in the standard view of the zwitterion, fragment values do, indicating that the charges are significantly delocalised over entire groups.

For saccharin, while there is no possibility of forming a zwitterion, there are some equally significant changes on co-crystallisation. In a similar fashion to piroxicam, saccharin was partitioned into separate molecular fragments, and the charges from experiment and theory are also given in Table 7. Here, the sulfurdioxide (D) group becomes more negative by 0.36 e, and the corresponding positive charge balance has been spread across the amide (E), and phenyl (F) groups, these becoming more positive by 0.20 and 0.31e respectively.

			
<b>Piroxicam</b>	(A)	(B)	(C)
Pv <b>(1)</b>	0.39	0.37	-0.3
Pv <b>(3)</b>	-0.88	0.63	0.19
$\Omega$ (exp) <b>(1)</b>	-0.16	0.68	-0.7
$\Omega$ (exp) <b>(3)</b>	-0.75	1.09	-0.36
$\Delta$ (Pv)	-1.27	0.26	0.49
$\Delta\Omega$ (exp)	-0.69	0.37	0.34

Saccharin	(D)	(E)	(F)
Pv (2)	0.17	-0.28	0.01
Pv (3)	-0.19	-0.08	0.32
$\Omega(\text{exp})$ (2)	0.40	-0.47	-0.01
$\Omega(\text{exp})$ (3)	0.37	-0.55	0.20
$\Delta(\text{Pv})$	-0.36	0.20	0.31
$\Delta\Omega(\text{exp})$	-0.03	-0.08	0.21

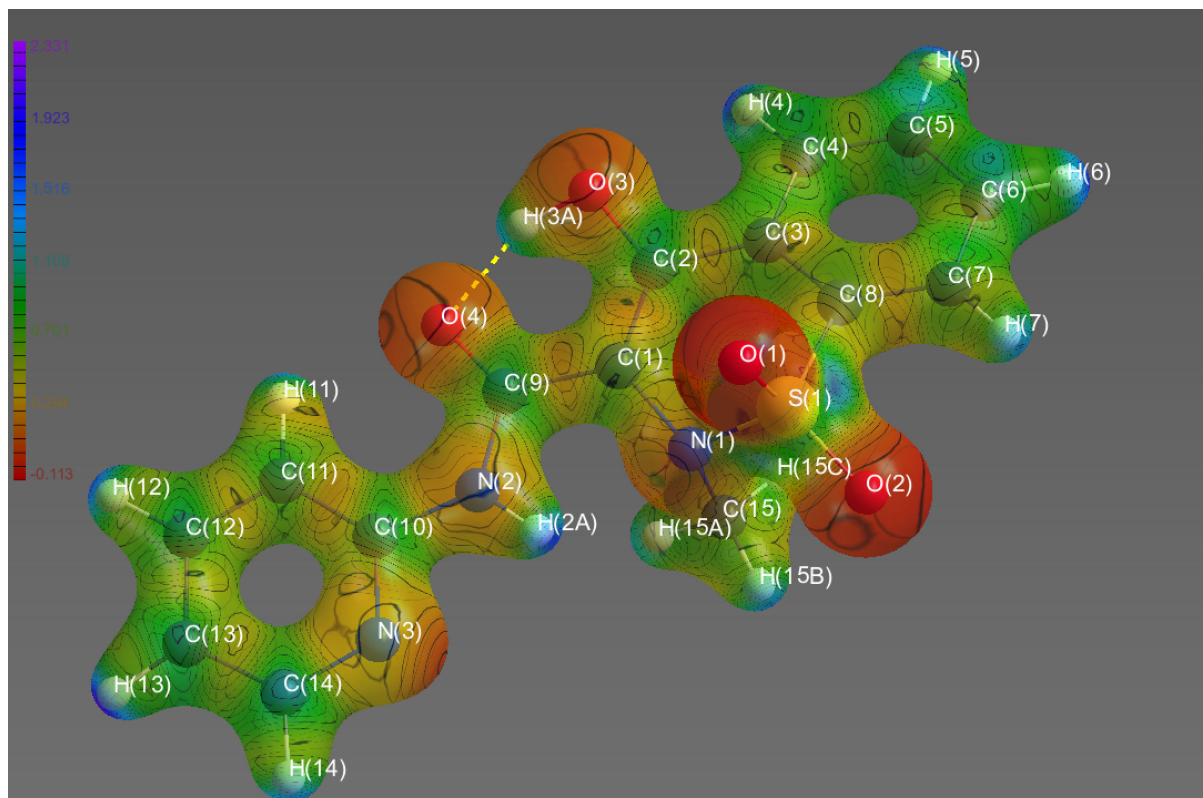
**Table 7** Atomic charges ( $e$ ) from multipole refinement.

### Electrostatic Potential

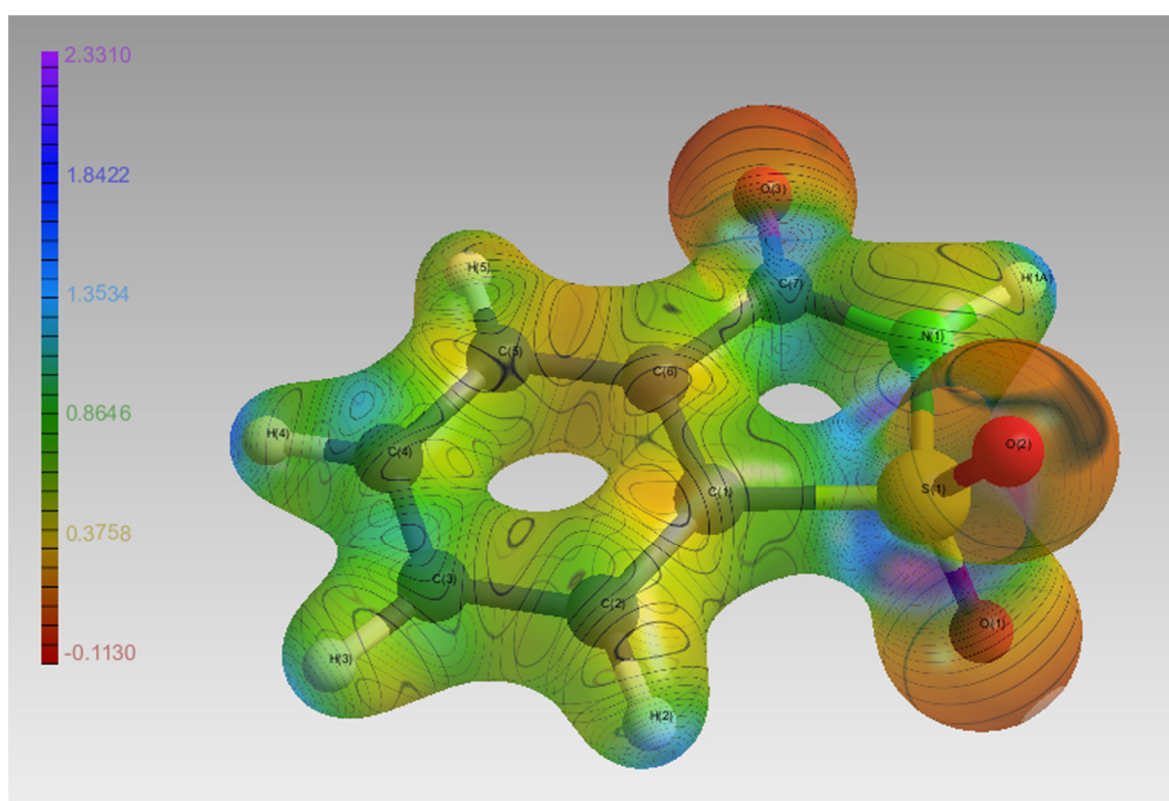
The major changes in EDD that are reflected in atomic charges should also be apparent in the molecular electrostatic potential (MEP), one of many chemical properties which can be derived from an analysis of electron density. The MEP is significant in EDD studies of co-crystal systems as it allows the visualisation of electron density across each molecule within the asymmetric unit, thus allowing visualisation of the non-covalent interactions which are the driving force in co-crystal formation.<sup>(16)</sup> Figure 9 shows the MEP calculated from the *Exp* refinement of (1), (2) and (3) respectively. MEP plots for isolated molecules exhibit strongly negative minima close to O atoms as well as pyridine N, as well as positive values near H-N groups and also close to S atoms. Formation of the co-crystal results in significant changes in the MEP of (3), broadly following the patterns observed in atomic charges discussed above. In particular, strongly positive values are now found in the vicinity of all hydrogens (C-H as well as N-H) on the protonated pyridine ring, while the negative MEP

associated with the formally deprotonated O(3') is substantially more negative in **(3)** than in **(1)**.

(a)



(b)



(c)

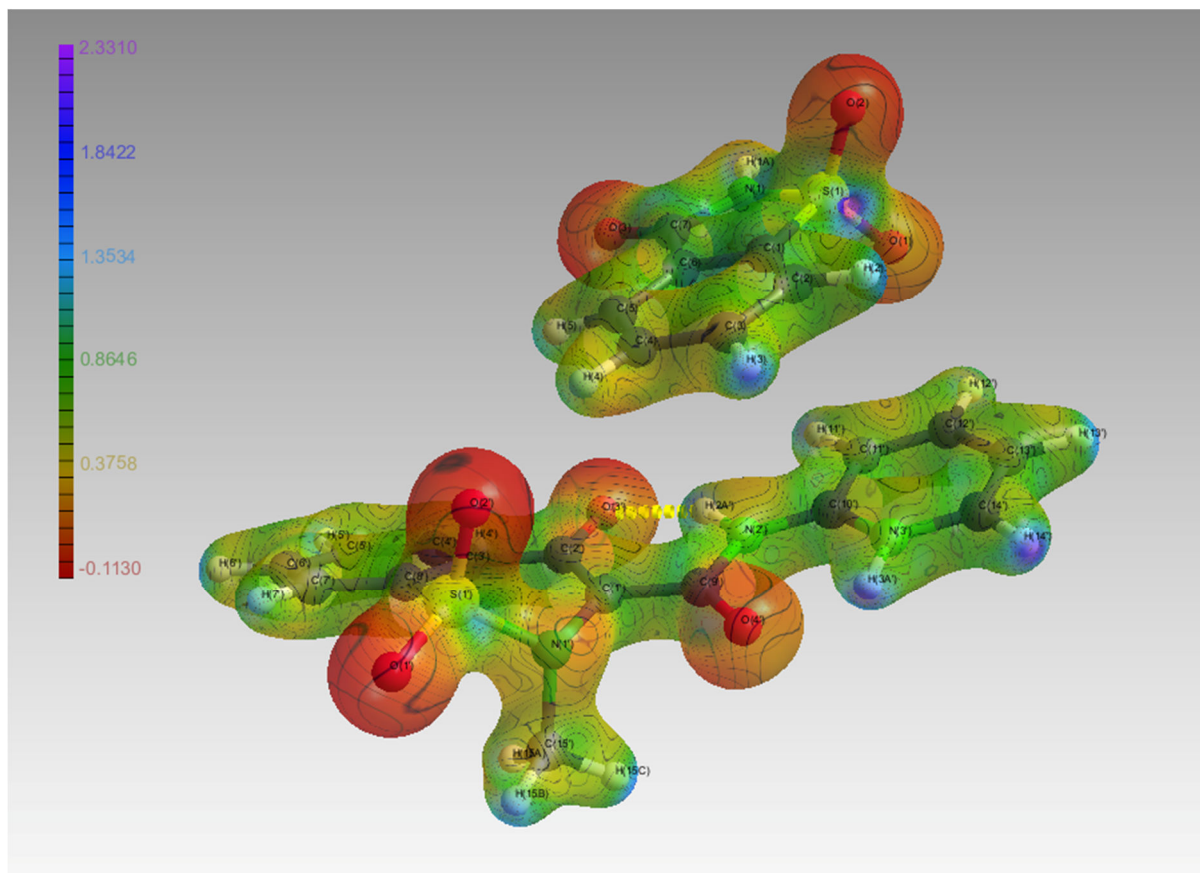


Figure 9: Molecular Electrostatic Potential of (1), (2) and (3) mapped onto an isosurface of  $\rho$ . The colour gradient ranges from  $2e/\text{bohr}$ , dark red (electropositive) through green and blue to  $32e/\text{bohr}$ , magenta (electronegative).

## Conclusions

We report an analysis of the experimental electron density distribution of the piroxicam-saccharin co-crystal, along with equivalent analysis of its pure constituents piroxicam and saccharin. The small differences in  $\rho$  and  $\nabla^2\rho$  values reported between experimental and theoretical studies, as well as the small residual errors that result from the multipole model, show that the models employed in the study are robust. Moreover, we found that the



introduction of ADPs for hydrogen atoms into the multipole model did not provide any improvements to the data obtained from multipole refinement from either of the complexes. A detailed investigation into the weak interactions in these systems, and especially the effects of co-crystallisation on the EDD and related phenomena within these complexes has been carried out. Specific co-crystal forces were assessed, such as the potential stabilising effect offered by saccharin, allowing piroxicam to adopt a different amide conformation, as well as a zwitterionic state in the co-crystal compared to the single crystal. A comparison of atomic charges and molecular electrostatic potential between **(1)**, **(2)** and **(3)** confirms that electron redistribution occurs during the co-crystallisation process to facilitate the formation of weak interactions which in turn stabilise the co-crystal system. Further work in this area will involve integration of the information gained from EDD studies with established synthetic techniques to engineer favourable weak interaction in order to drive the development of more efficacious pharmaceutical co-crystals.

## Acknowledgements

DEH would like to thank The University of Sydney Bridging Support Scheme for funding.

## References

1. Rossi S. Australian Medicines Handbook 2014 (online). Adelaide: Australian Medicines Handbook Pty. Ltd; 2014.
2. Scarpignato C. Piroxicam- $\beta$ -Cyclodextrin: A GI Safer Piroxicam. *Current Medicinal Chemistry*. 2013;20(19):2415-37.
3. Banerjee R, Bhatt PM, Ravindra NV, Desiraju GR. Saccharin Salts of Active Pharmaceutical Ingredients, Their Crystal Structures, and Increased Water Solubilities. *Cryst Growth Des*. 2005;5(6):2299-309.
4. Sekhon BS. Drug-drug co-crystals. *Daru, J Pharm Sci*. 2012;20:45.
5. Springuel G, Norberg B, Robeyns K, Wouters J, Leyssens T. Advances in Pharmaceutical Co-crystal Screening: Effective Co-crystal Screening through Structural Resemblance. *Cryst Growth Des*. 2012;12(1):475-84.
6. Qiao N, Li M, Schindwein W, Malek N, Davies A, Trappitt G. Pharmaceutical cocrystals: An overview. *Int J Pharm*. 2011;419(1-2):1-11.

7. Desiraju GR. Chapter 1. Pharmaceutical Salts and Co-crystals: Retrospect and Prospects. 2011:1-8.
8. Bader RFW. Atoms in Molecules: A Quantum Theory: Oxford Univ. Press; 1994. 454 pp. p.
9. Nguyen TH, Howard ST, Hanrahan JR, Groundwater PW, Platts JA, Hibbs DE. Experimental and Theoretical Charge Density Distribution in a Host-Guest System: Synthetic Terephthaloyl Receptor Complexed to Adipic Acid. *J Phys Chem A*. 2012;116(23):5618-28.
10. Nguyen TH, Groundwater PW, Platts JA, Hibbs DE. Experimental and Theoretical Charge Density Studies of 8-Hydroxyquinoline Cocrystallized with Salicylic Acid. *J Phys Chem A*. 2012;116(13):3420-7.
11. Chatteraj S, Shi L, Chen M, Alhalaweh A, Velaga S, Sun CC. Origin of Deteriorated Crystal Plasticity and Compaction Properties of a 1:1 Cocrystal between Piroxicam and Saccharin. *Cryst Growth Des*. 2014: Ahead of Print.
12. Bordner J, Richards JA, Weeks P, Whipple EB. Piroxicam monohydrate: a zwitterionic form, C<sub>15</sub>H<sub>13</sub>N<sub>3</sub>O<sub>4</sub>S.H<sub>2</sub>O. *Acta Crystallogr, Sect C: Cryst Struct Commun*. 1984;C40(6):989-90.
13. Bart JCI. Crystal and molecular structure of saccharin. *J Chem Soc B*. 1968(4):376-82.
14. Aakeroy CB, Salmon DJ. Building co-crystals with molecular sense and supramolecular sensibility. *CrystEngComm*. 2005;7:439-48.
15. Desiraju GR. Supramolecular synthons in crystal engineering - a new organic synthesis. *Angew Chem, Int Ed Engl*. 1995;34(21):2311-27.
16. Gellman SH. Introduction: Molecular Recognition. *Chem Rev (Washington, D C)*. 1997;97(5):1231-2.
17. Farrugia LJ. ORTEP-3 for windows - a version of ORTEP-III with a graphical user interface (GUI). *J Appl Crystallogr*. 1997;30(5, Pt. 1):565.
18. Oxford D. *CrysAlis<sup>Pro</sup>*. 1.171.37.31b ed. Abingdon, England: Oxford Diffraction Ltd; 2006.
19. Sheldrick GM. A short history of SHELX. *Acta Crystallogr, Sect A: Found Crystallogr*. 2008;64(1):112-22.
20. Allen FH, Kennard O, Watson DG, Brammer L, Orpen AG, Taylor R. Tables of bond lengths determined by x-ray and neutron diffraction. Part 1. Bond lengths in organic compounds. *J Chem Soc, Perkin Trans 2*. 1987(12):S1-S19.
21. Volkov A, Macchi P, Farrugia LJ, Gatti C, Mallinson P, Richter T, et al. XD2006- a computer program for multipole refinement, topological analysis of charge densities and evaluation of intermolecular energies from experimental or theoretical structure factors. 2006.
22. Hansen NK, Coppens P. Electron population analysis of accurate diffraction data. VI. Testing aspherical atom refinements on small-molecule data sets. *Acta Crystallogr, Sect A*. 1978;A34(6):909-21.
23. Hibbs DE, Austin-Woods CJ, Platts JA, Overgaard J, Turner P. Experimental and theoretical charge density study of the neurotransmitter taurine. *Chem - Eur J*. 2003;9(5):1075-84.
24. Hibbs DE, Hanrahan JR, Hursthouse MB, Knight DW, Overgaard J, Turner P, et al. Experimental and theoretical charge distribution in (Z)-N-methyl-C-phenylnitron. *Org Biomol Chem*. 2003;1(6):1034-40.
25. Schmokel MS, Cenedese S, Overgaard J, Jorgensen MRV, Chen YS, Gatti C, et al. *Inorganic Chemistry*. 2012;51:8607-16.
26. Du JJ, Overgaard J, Williams PA, Platts JA, Hibbs DE. in preparation.
27. Clementi E, Raimondi DL. Atomic Screening Constants from SCF Functions. *The Journal of Chemical Physics*. 38:2686-9.
28. Hirshfeld FL. Can x-ray data distinguish bonding effects from vibrational smearing? *Acta Crystallogr, Sect A*. 1976;A32, Pt. 2:239-44.
29. Hoser AA, Dominiak PM, Wozniak K. Towards the best model for H atoms in experimental charge-density refinement. *Acta Crystallogr, Sect A: Found Crystallogr*. 2009;65(4):300-11.

30. Madsen AO, Sorensen HO, Flensburg C, Stewart RF, Larsen S. Modeling of the nuclear parameters for H atoms in X-ray charge-density studies. *Acta Crystallogr, Sect A: Found Crystallogr.* 2004;A60(6):550-61.
31. Madsen AO. SHADE web server for estimation of hydrogen anisotropic displacement parameters. *J Appl Crystallogr.* 2006;39(5):757-8.
32. Frisch MJ, Trucks GW, Schlegel HB, Scuseria GE, Robb MA, Cheeseman JR, et al. Gaussian09. 2006.
33. Becke AD. A new mixing of Hartree-Fock and local-density-functional theories. *J Chem Phys.* 1993;98(2):1372-7.
34. Lee C, Yang W, Parr RG. Development of the Colle-Salvetti correlation-energy formula into a functional of the electron density. *Phys Rev B: Condens Matter.* 1988;37(2):785-9.
35. Keith TA. AIMAll. 14.06.21 ed. Overland Park KS, USA: TK Gristmill Software; 2014.
36. Kojic-Prodic B, Ruzic-Toros Z. Structure of the antiinflammatory drug 4-hydroxy-2-methyl-N-2-pyridyl-2H-1λ6,2-benzothiazine-3-carboxamide 1,1-dioxide (piroxicam). *Acta Crystallogr, Sect B.* 1982;B38(11):2948-51.
37. Bhatt PM, Ravindra NV, Banerjee R, Desiraju GR. Saccharin as a salt former. Enhanced solubilities of saccharinates of active pharmaceutical ingredients. *Chem Commun (Cambridge, U K).* 2005(8):1073-5.
38. Spackman MA. Molecular electric moments from x-ray diffraction data. *Chem Rev.* 1992;92(8):1769-97.
39. Spackman MA. Hydrogen bond energetics from topological analysis of experimental electron densities: Recognising the importance of the promolecule. *Chem Phys Lett.* 1999;301(5,6):425-9.
40. Spackman MA, Byrom PG, Alfredsson M, Hermansson K. Influence of intermolecular interactions on multipole-refined electron densities. *Acta Crystallogr, Sect A: Found Crystallogr.* 1999;A55(1):30-47.
41. Koritsanszky TS, Coppens P. Chemical applications of x-ray charge-density analysis. *Chem Rev (Washington, D C).* 2001;101(6):1583-627.
42. Coppens P. *X-Ray Charge Densities and Chemical Bonding* New York: Oxford University Press 1997.
43. Du JJ, Váradi L, Tan J, Zhao Y, Groundwater PW, Platts JA, et al. Experimental and Theoretical Charge Density Distribution in Pigment Yellow 101 (*in press*). *Physical Chemistry and Chemical Physics.* 2015.
44. Koch U, Popelier PLA. Characterization of C-H-O Hydrogen Bonds on the Basis of the Charge Density. *J Phys Chem.* 1995;99(24):9747-54.
45. Macrae CF, Bruno IJ, Chisholm JA, Edgington PR, McCabe P, Pidcock E, et al. Mercury CSD 2.0 - New Features for the Visualization and Investigation of Crystal Structures. *Journal of Applied Crystallography.* 2008(41):466-70.
46. Abramov YA. On the possibility of kinetic energy density evaluation from the experimental electron-density distribution. *Acta Crystallogr, Sect A: Found Crystallogr.* 1997;A53(3):264-72.
47. Espinosa E, Molins E, Lecomte C. Hydrogen bond strengths revealed by topological analyses of experimentally observed electron densities. *Chem Phys Lett.* 1998;285(3,4):170-3.
48. Ziólkowski M, Grabowski SJ, Leszczynski J. *Journal of Physical Chemistry A.* 2006;119.